α Cluster Structure and Resonance States of ^{13}C

炭素13のアルファクラスター構造と共鳴状態

Seungheon Shin

A dissertation submitted for the degree of

Doctor of Philosophy

Department of Cosmosciences

Graduate School of Science

Hokkaido University

March 2023

Abstract

Carbon isotopes have attracted great interest and have been important subjects in nuclear physics as they exhibit a rich variety of cluster phenomena. The Hoyle state, the 0_2^+ state of ^{12}C, has a very interesting clustering aspect; Bose-Einstein condensate (BEC) of the three α particles. In the recent two decades, the structure of the Hoyle state and its analogous states in neighboring nuclei have been a major topic. ^{13}C is one of the particularly important nuclei as the system can be described as three α particles (bosons) with a valence nucleon (fermion). The BEC of the three α particles with a neutron as an impurity, which is referred to as the Hoyle-analog state, and the predominant α cluster states in ^{13}C are the main interests. For example, ^{13}C as the $3\alpha + n$ system exhibits the evidence of the triangular symmetry of the 3α particles with the spinor effect accompanied by the valence neutron, in which the triangular symmetry successfully predicted rotational bands and excited states in ^{12}C.

In my thesis, the band structures and resonance states of ^{13}C are studied. The real-time evolution method (REM), which uses the equation-of-motion of clusters, has been applied. First, the symmetry of ^{13}C is investigated in comparison with the study by Bijker *et al.* [Phys. Rev. Lett. 122, 162501 (2019)], which explained the rotation-vibration spectrum of ^{13}C by assuming a triangular nuclear shape of 3α particles with a neutron. REM is a full microscopic nuclear model that does not assume any nuclear shape. As a result, REM described the low-lying states more accurately than the previous studies. The wave functions are analyzed to understand the shape of each state and showed that the ground band has a triangular symmetry,

while the other excited bands do not.

In subsequent, the Hoyle-analog state in ^{13}C, the three α plus one neutron condensate, is investigated. It is still under debate which state is the Hoyle-analog state in ^{13}C. Several experimental studies showed that the $1/2^-$ states exhibit strong cluster aspects that can be the Hoyle-analog state, while other theoretical studies concluded that there is no Hoyle-analog state in the $1/2^-$ states. In order to figure out the Hoyle-analog state and deal with the resonance states located around the $3\alpha + n$ threshold, the analytic continuation in the coupling constant (ACCC) is introduced. ACCC with REM properly estimated the resonance states of the $1/2^-$ states together with their characteristics such as the radii and monopole transition probabilities. This study suggests that the $1/2^-_4$ state can be the possible candidate for the Hoyle-analog state in ^{13}C revealing large spatial excitation and transition strength as the signature of the Hoyle state.

Contents

Chapter 1

Introduction

1.1 α clustering in light nuclei and the Hoyle state

There are several astrophysical reaction scenarios in the universe that explain how and where the elements are made. One of the most important reactions is the triple-α process occurring in stars. In this process, the fusion of two α particles is followed by the capture of another α particle to form the resonance state in ^{12}C. This 3α state decays into the ground state of ^{12}C, and it explains the abundance of ^{12}C in the universe. The resonant 3α state is an excited state of ^{12}C which was first predicted by Fred Hoyle [1] and hence, called the Hoyle state. The Hoyle state is an α cluster state which cannot be explained by the traditional shell model calculations as shown in Figure 1.1. The first column shows the experiment and the others are the shell model calculations. The blue state is the Hoyle state (the second 0^+ state of ^{12}C) and the shell models cannot reproduce it as shown in the red-dashed blank area.

The Hoyle state is a key state in other reactions to explain how heavier elements are made. Thus, it is essential to investigate the properties of the Hoyle state. To date, there are two different ways that explain the structure of the Hoyle state. One is that the Hoyle state can be regarded as a Bose-Einstein condensate (BEC) of 3α particles [2]. Figure 1.2 would provide an illustrative understanding of the Hoyle state as a BEC. The 3α particles occupy the same S orbit within the dilate

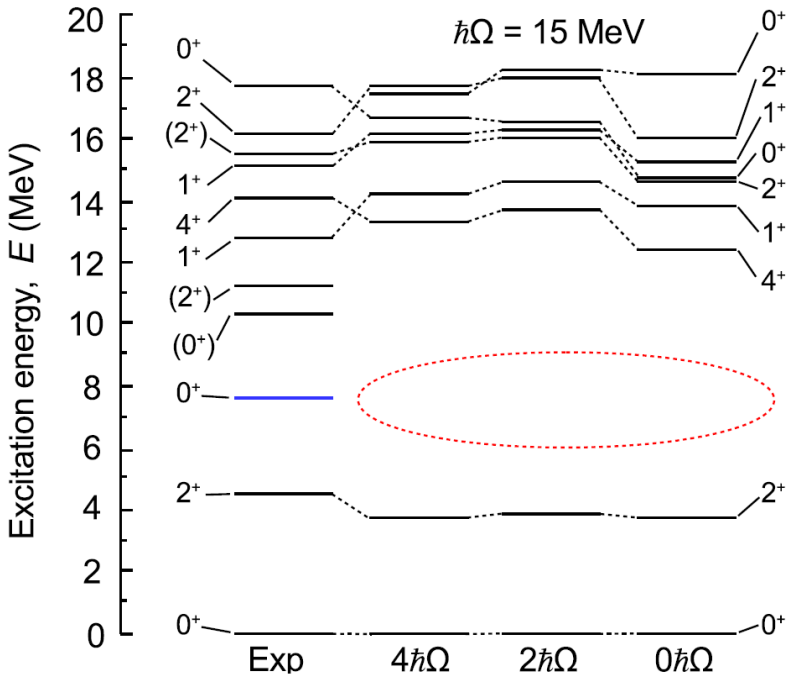

Figure 1.1: The ^{12}C energy spectrum. The first column shows the experiment and the others are the shell model calculations. The blue state is the Hoyle state and the shell models cannot reproduce it. The figure was taken from Ref. [3].

harmonic oscillator potential. Meanwhile, the two protons and two neutrons are strongly bound as an α particle occupying the same s orbit within the α particle. This Hoyle state as a BEC exhibits some particular signatures such as a very large radius (>3.4 fm) compared to the ground state (2.4 fm) as a dilute nature and a strong monopole transition probability to the ground state.

This novel α cluster phenomenon triggered great interest. For example, the studies have been extended to BEC in many α particle systems such as 4α and 5α condensation in ^{16}O [4, 5] and ^{20}Ne [6]. Also, the analogous states of the Hoyle state in neighboring nuclei have been one of the major topics. For example, in the highly excited energy region of carbon isotopes, a different type of clustering that is the linear-chain of alpha particles has also been actively discussed [7–12].

Among the carbon isotopes, ^{13}C is one of the particularly important nuclei as the system can be described as three α particles (bosons) with a valence nucleon (fermion). The BEC of the three α particles with a neutron as an impurity, which

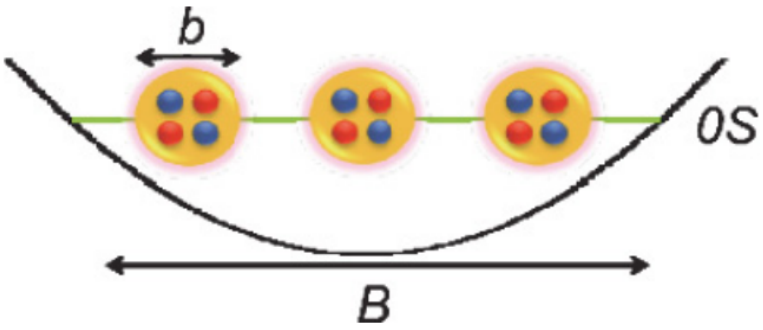

Figure 1.2: The Hoyle state where the α particles occupy the same S orbit within the dilate harmonic oscillator potential B, while the two protons and two neutrons are bound as an α particle occupying the same s orbit within the α particle oscillator b. The figure was taken from Ref. [19].

is referred to as the Hoyle-analog state, and the predominant α cluster states in ^{13}C are the main interests in this work [13–18].

1.2 Resonance and Hoyle-analog state in ^{13}C

The Hoyle-analog state is a condensate state of the Hoyle state with other particles such as neutrons and protons. In ^{13}C, the Hoyle-analog state is a $3\alpha + n$ condensate state. Since the Hoyle state is the 3α particle state occupying the same S orbit, the Hoyle-analog state in ^{13}C is expected to have the lowest orbits of the valence neutron coupled to the Hoyle state:

$$^{12}\mathrm{C}(0_2^+) \otimes s\text{-wave neutron} \rightarrow \ ^{13}\mathrm{C}(1/2^+), \tag{1.1}$$

$$^{12}\mathrm{C}(0_2^+) \otimes p\text{-wave neutron} \rightarrow \ ^{13}\mathrm{C}(1/2^-, 3/2^-). \tag{1.2}$$

It is still under debate which state is the Hoyle-analog state in ^{13}C. Several experimental studies showed that the $1/2^-$ states exhibit strong cluster aspects that imply the Hoyle-analog state [18, 20] while other theoretical studies concluded that there is no Hoyle-analog state in the $1/2^-$ states. The antisymmetrized molecular dynamics (AMD) [17] and the orthogonality condition model (OCM) [21] calculations argue that the Hoyle-analog state is in the $1/2^+$ states. In order to figure out which state

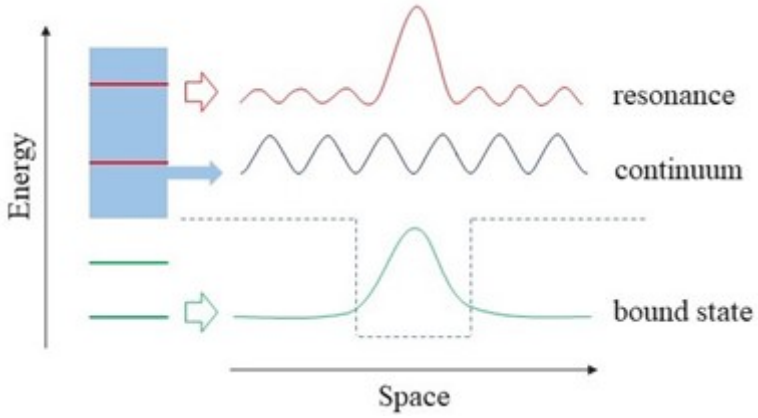

Figure 1.3: Schematic illustration of wave functions of the bound state, continuum state, and resonance state. The figure was partially reproduced from Ref. [23].

and where is the Hoyle-analog state in ^{13}C, the excited energy region around the $3\alpha + n$ threshold is focused as suggested by K. Ikeda *et al.* [22], in which a cluster formation in a nucleus appears around the threshold of its cluster units. However, there are several thresholds below the $3\alpha + n$ threshold in ^{13}C such as the $^{12}\mathrm{C} + n$ and $^{9}\mathrm{Be} + \alpha$ thresholds. They make the bound state approximation not applicable to the calculated excited states due to the contamination of the continuum states.

Figure 1.3 shows schematic concepts of the bound state, continuum state, and resonance state in a potential. The wave function of a bound state is drawn as green curve. In the bound states, nucleons are interacting with each other, and they are confined in the interacting area in which the wave function has a large amplitude. The continuum states appear above the particle decay thresholds, and their wave function is spread out in whole space in the time-independent formalism of quantum mechanics. The resonance states exist in the continuum region, but the particles are interacting with each other like the bound states. They have complex energies where the imaginary parts represent decay widths, so their amplitudes of the time-dependent wave function decrease with time. This decay property is drawn as the amplitudes outside of the interacting area. It makes the resonance states difficult to study because the wave functions resemble the continuum states and thus are easily contaminated by the continuum states.

In order to identify the resonant states from the non-resonant continuum states,

the analytic continuation in the coupling constant (ACCC) [24, 25] is introduced. The resonant states are analytically continued from the bound states which are calculated with the Hamiltonian including an attractive potential. In this study, ACCC is combined with the real-time evolution method (REM) [26] as explained in Chapter 2. In Chapter 3 the benchmark calculations are performed to confirm the validity of ACCC with REM. Then, the framework of ACCC with REM is applied to the resonance states in ^{13}C.

1.3 Symmetry of nuclear shape in light nuclei

Apart from the studies of α condensation, symmetry is another interpretation of the α clustering in light nuclei. Symmetry plays an important role in respect of the law of physics. Some simple symmetry structures of α particles and their vibrations are shown in Figure 1.4: ^{8}Be as a dumbbell shape and ^{12}C as a triangle shape. The excited states of the nuclei with such symmetry assumption are explained by the vibration modes as depicted with arrows in the figure and their rotations.

For example, a study of ^{12}C applying the algebraic cluster model (ACM) [27–29], which assumes a triangular shape of 3α particles, explained excited states by the rotation of different vibrational modes of the triangle. The ground state (0^+_1) is a compact 3α particle structure and the excited states that can be explained by the rotation of this structure are classified into the ground state rotational band as shown in Figure 1.5. The horizontal axis is $J(J+1)$ with the angular momentum J. The energy is proportional to $J(J+1)$ and the inverse of the gradient is related to the moment of inertia. This symmetry model predicted that the 4^+ state in the ground state band is degenerate parity doublet states with the 4^- state and predicted a new member to be the 5^- state in the ground state band [27]. These predictions were confirmed by the experiment [30]. This triangle shape also explained the experimentally measured strong electric quadrupole ($E2$) transition probability of the 2^+_1 state to the ground state, which indicates the same structure in the rotational band. From such pieces of evidence, the ground state band can be interpreted as a

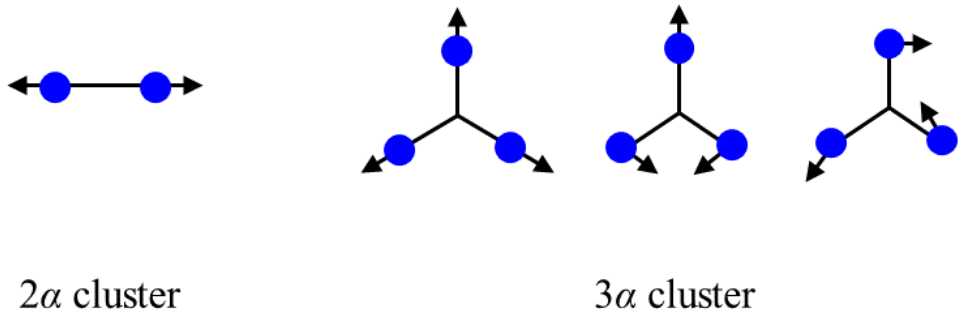

Figure 1.4: Simple symmetry structures of 2α and 3α particles and their vibrations are shown.

compact 3α particle structure, in which the member states can be approximated by a single basis wave function.

ACM also explained the Hoyle state as a vibration of 3α particles and classified some other excited states as the Hoyle state rotational band having the same vibration mode as the Hoyle state. However, they failed to explain the strong monopole transition probability of the Hoyle state (0_2^+) and it is understandable when the Hoyle state is interpreted as a BEC state. The Hoyle state is a superposition of many different configurations of 3α particles and thus the symmetry model assuming a specific nuclear shape deviates from the nature of the Hoyle state.

The study of the triangular symmetry in ^{12}C was extended to ^{13}C where the triangular symmetry of 3α particles with an additional neutron was assumed [31]. In Figure 1.6, the ground state ($1/2^-$) rotational band (blue bands) with the other two bands, which have the same rotation structure, was proposed together with the $1/2^+$ rotational band (black band) having a different structure with the valence neutron as shown. They compared their calculated energy spectrum with the available experimental data and reproduced some measured strong $E2$ transition probabilities in the ground band as in the ^{12}C case, and hence, they argued that ^{13}C shows triangular symmetry of 3α particles with a single neutron.

Such triangular symmetry suggests an interesting insight into the structure of carbon isotopes, which contradicts the BEC interpretation of the Hoyle state and its

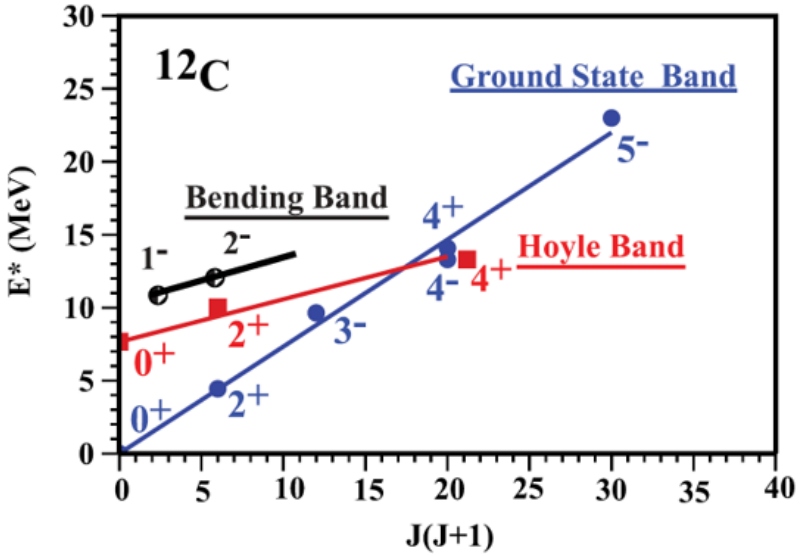

Figure 1.5: Ground band and Hoyle band in ^{12}C explained by triangular symmetry of 3α particles. The figure was taken from Ref. [30].

analogous states. However, it must be tested if symmetry in ^{13}C, which is considered to be hindered by the motion of the valence neutron, is exhibited in reality by the microscopic models without any assumption of the nuclear shape [32]. The symmetry model presumes a nuclear shape so that it naturally cannot examine the symmetry structures and the deviation from them. Indeed, the ^{13}C energy spectrum calculated by ACM shows several overestimated states in the high spin states.

1.4 Purpose

The real-time evolution method (REM) recently proposed by Imai *et al.* [26] is one of the microscopic cluster models which can examine the shape of nuclei without any assumption of symmetry. It generates basis wave functions with various cluster configurations as time evolves by using the equation-of-motion (EOM) of the Gaussian wave packets. A benchmark calculation showed that REM precisely describes the 3α system including the Hoyle state as shown in Figure 1.7. It is noted that REM superposes a massive number of the basis wave functions to describe the cluster systems, and it does not introduce any assumption about the symmetry of nuclear shape and cluster configurations. Therefore, REM is a suitable nuclear model to test

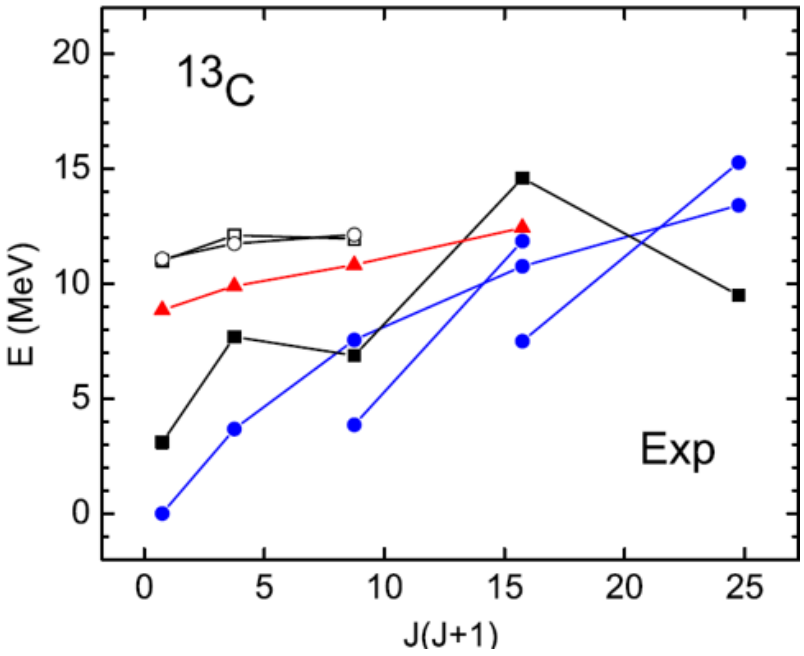

Figure 1.6: Rotation-vibration band structure in ^{13}C explained by triangular symmetry of $3\alpha + n$. The figure was taken from Ref. [31].

if there exists any symmetry in nuclei as well as to describe various configuration superposed states like the Hoyle state.

The first aim of this work is to verify the triangular symmetry in ^{13}C as the $3\alpha + n$ system. For this purpose, the electric quadrupole transition probabilities between the states in the energy spectrum calculated by REM are investigated since a strong E2 transition can be evidence of band structures. In addition, each state in the spectrum is analyzed by overlapping with a single-basis wave function to see which configuration is the representative shape for each state.

In subsequence, the resonance states in ^{13}C are investigated to search for the Hoyle-analog state using ACCC with REM as explained in Section 1.2. Some candidates for the Hoyle-analog state in ^{13}C were roughly reported in the highly excited region within the REM framework (Figure 1.8) [33]. Therefore, the second aim is to identify the resonance states in ^{13}C and figure out which state can be regarded as the Hoyle-analog state from them. The $1/2^-$ states are mainly studied because several experimental studies reported that there are well-developed cluster states implying one of them could be the Hoyle-analog state by measuring the isoscalar monopole

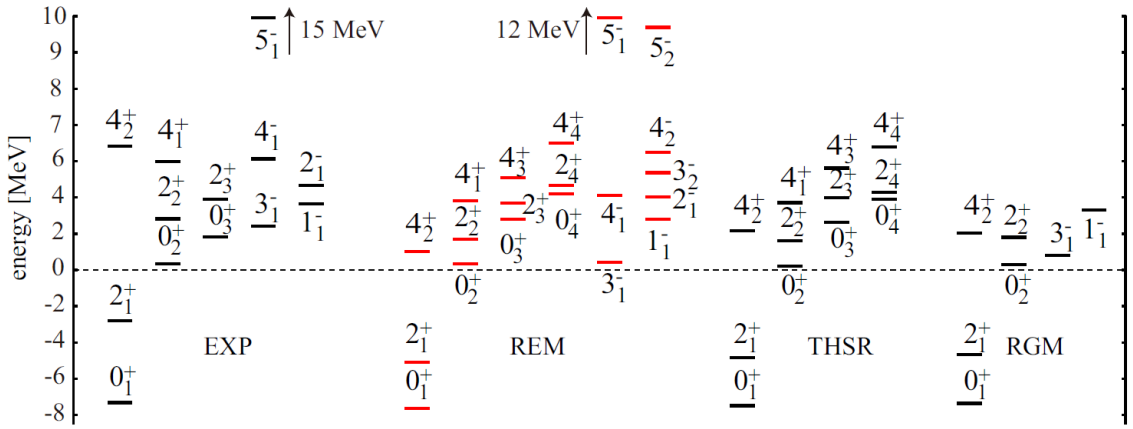

Figure 1.7: Energy spectrum of ^{12}C compared with the experiment and other theoretical models. The figure was taken from Ref. [26].

($IS0$) transition probabilities. Thus, the $IS0$ transitions are investigated within the framework of ACCC with REM, in which the strong transition probability is the signature of the Hoyle state, together with investigating the radii of each state to confirm a large radius as the dilute nature of the Hoyle state.

This thesis is organized as follows. In Chapter 2, the theoretical frameworks to study ^{13}C are elucidated. The results are shown and discussed in Chapter 3. Firstly, the α cluster structures of the low-lying states are discussed with the comparison of rotation bands and their intrinsic shapes. Secondly, the resonance states are discussed with the practical development of the ACCC method combined with REM. The candidate of the Hoyle analog state is finally proposed. In the final chapter, the study on ^{13}C is summarized.

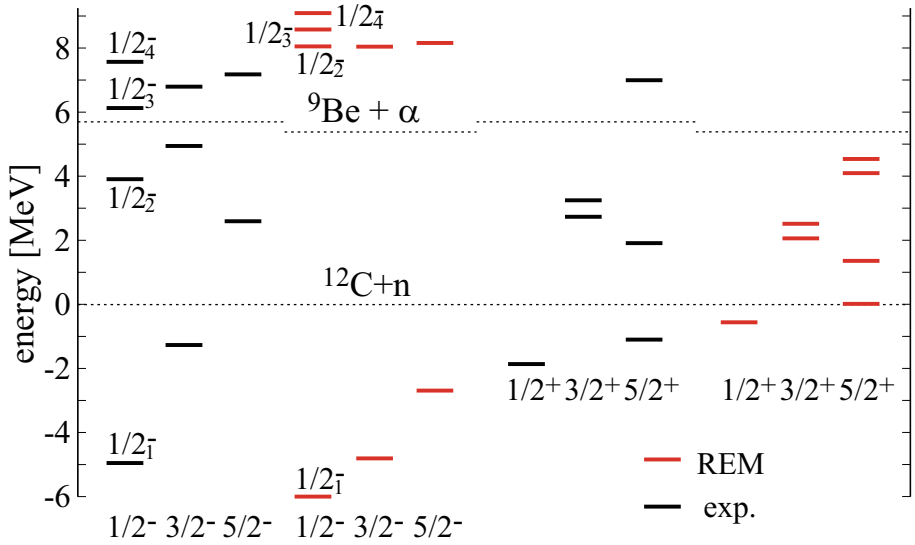

Figure 1.8: Some rough candidates for the Hoyle-analog state in ^{13}C using REM. The figure was taken from Ref. [33].

Chapter 2

Theoretical framework

2.1 Basis wave function for $N\alpha$+1 particles system and Hamiltonian

In this section, we first see the Hamiltonian and the framework of the $N\alpha + 1$ microscopic cluster model. The Hamiltonian for the $N\alpha + 1$ nuclear system is given as,

$$\hat{H} = \sum_{i=1}^{4N+1} \hat{t}_i - \hat{t}_{cm} + \sum_{i<j}^{4N+1} \hat{v}_N(r_{ij}) + \sum_{i<j}^{4N+1} \hat{v}_C(r_{ij}), \tag{2.1}$$

where $\hat{t}_i$ and $\hat{t}_{cm}$ denote the kinetic energies of the ith nucleon and the center-of-mass, respectively. The $\hat{v}_N$ and $\hat{v}_C$ are the effective nucleon-nucleon interaction and Coulomb interaction. The nucleon-nucleon interaction $\hat{v}_N$ includes the central force of Volkov No. 2 [34] and the spin-orbit interaction of the G3RS force [35] as,

$$\begin{aligned}\hat{v}_N =& \sum_{n=1}^{2} v_n e^{-r_{ij}^2/\alpha_n^2}(W + BP_\sigma - HP_\tau - MP_\sigma P_\tau) \\ &+ \sum_{n=1}^{2} u_n e^{-\beta_n r_{ij}^2} \boldsymbol{l}\cdot\boldsymbol{s} P(^3O),\end{aligned} \tag{2.2}$$

$$P(^3O) = \frac{1+P_\sigma}{2}\frac{1+P_\tau}{2}, \tag{2.3}$$

in which the Majorana parameter is $M = 0.6$ with $W = 0.4$, $B = H = 0.125$ and the parameter $v_1 = -60.65$, $v_2 = 61.14$ MeV and $\alpha_1 = 1.80$, $\alpha_2 = 1.01$ fm^2. The strength of the spin-orbit interaction is $u_1 = -u_2 = 2000$ MeV with $\beta_1 = 5.0$, $\beta_2 = 2.778$ fm^2. $P(^3O)$ is the projector onto the triplet state where P_σ and P_τ are spin and isospin exchange operators, respectively. The Majorana parameter and the spin-orbit strength will be changed when the resonance states of ^{13}C are discussed and their values are detailed later.

As for the wave function of the $N+1$ particles system composed of $N\alpha$ particles and a valence neutron, we use the Brink-Bloch wave function [36], which describes an α particle having $(0s)^4$ configuration and the valence nucleon,

$$\Phi(\boldsymbol{Z}_1, ..., \boldsymbol{Z}_{N+1}) = \mathcal{A}\left\{ \Phi_\alpha(\boldsymbol{Z}_1) \cdots \Phi_\alpha(\boldsymbol{Z}_N)\phi_n(\boldsymbol{Z}_{N+1}) \right\}, \tag{2.4}$$

$$\Phi_\alpha(\boldsymbol{Z}) = \mathcal{A}\left\{ \phi(\boldsymbol{r}_1, \boldsymbol{Z})\chi_{p\uparrow} \cdots \phi(\boldsymbol{r}_4, \boldsymbol{Z})\chi_{n\downarrow} \right\}, \tag{2.5}$$

$$\Phi_n(\boldsymbol{Z}) = \phi(\boldsymbol{r}, \boldsymbol{Z})\chi_{n\uparrow}, \tag{2.6}$$

$$\phi(\boldsymbol{r}, \boldsymbol{Z}) = \left(\frac{2\nu}{\pi}\right)^{3/4} \exp\left\{ -\nu\left(\boldsymbol{r} - \boldsymbol{Z}\right)^2 \right\}, \tag{2.7}$$

in which $\Phi_\alpha(\boldsymbol{Z})$ and $\Phi_n(\boldsymbol{Z})$ represent the wave packets of the α cluster and the valence nucleon located at $\boldsymbol{Z}$, respectively. In this study, we set the spin down fixed for the last neutron in Eq. (2.6). The set of the three-dimensional vectors $\{\boldsymbol{Z}_1, ..., \boldsymbol{Z}_{N+1}\}$ is complex numbered and each set describes the $3\alpha + n$ cluster positions by the real numbers and their momenta by the imaginary numbers in the phase space. Here, one α particle consists of four nucleons, which are assumed to be located at the same position $\boldsymbol{Z}$, so it is easy to treat the nuclear system as a cluster structure. The α particle width parameter $\nu = 1/(2b^2)$ is fixed to have $b = 1.46$ fm [37] for ^{13}C.

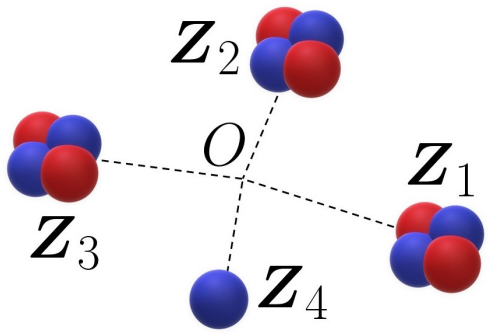

Figure 2.1: Schematic of the $3\alpha + n$ system of REM.

2.2 Generator coordinate method

The generator coordinate method is a method superposing generating functions $\Phi(a)$. The real or complex parameters $\{a|a = a_1, a_2, ..., a_i, ...\}$ denote the particle coordinates and are called generator coordinates. The GCM wave function Ψ is constructed by a linear superposition of the generating functions [38],

$$\Psi = \int da f(a)\Phi(a), \tag{2.8}$$

where $f(a)$ is a weight function. It is noted that generating wave functions are usually not orthogonal to each other. We obtain the GCM wave function by superposing the intrinsic wave functions with different sets of $\{\boldsymbol{Z}_1, ..., \boldsymbol{Z}_{N+1}\}$ of various configurations after the parity and angular momentum projection. The GCM wave function for the $N\alpha + 1$ particles system will be the form of

$$\Psi^{J\pi}_M = \sum_K \int d^3Z_1 ... d^3Z_{N+1} f_K(\boldsymbol{Z}_1, ..., \boldsymbol{Z}_{N+1}) \hat{P}^{J\pi}_{MK} \Phi(\boldsymbol{Z}_1, ..., \boldsymbol{Z}_{N+1}), \tag{2.9}$$

where Φ is the Brink wave function of Eq. (2.4) and $f_K(\boldsymbol{Z}_1, ..., \boldsymbol{Z}_{N+1})$ is the superposition amplitude. $\hat{P}^{J\pi}_{MK}$ is the parity and the angular momentum projection operator

of the form

$$\hat{P}^{\pi} = \frac{1+\pi\hat{P}_x}{2}, \quad \pi = \pm, \tag{2.10}$$

$$\hat{P}^{J}_{MK} = \frac{2J+1}{8\pi^2}\int d\Omega \mathcal{D}^{J*}_{MK}(\Omega)\hat{R}(\Omega). \tag{2.11}$$

In our numerical calculations, Eq. (2.9) is approximately discretized by a sum of the finite number $p_{\max}$ of the basis wave functions,

$$\Psi^{J\pi}_{M} = \sum_{p=1}^{p_{\max}}\sum_{K=-J}^{J} f_{pK}\hat{P}^{J\pi}_{MK}\Phi(\boldsymbol{Z}^{(p)}_1, ..., \boldsymbol{Z}^{(p)}_{N+1}), \tag{2.12}$$

where the pth set of the vectors $\{\boldsymbol{Z}_1, ..., \boldsymbol{Z}_{N+1}\}$ is denoted as $\boldsymbol{Z}^{(p)}_1, ..., \boldsymbol{Z}^{(p)}_{N+1}$ and the amplitude f_{pK} and the energies are determined by the Hill-Wheeler equation [39],

$$\sum_{p,K} H^{J^\pi}_{p'K'pK} f_{pKn} = E^{J^\pi}_n \sum_{p,K} N^{J^\pi}_{p'K'pK} f_{pKn}, \tag{2.13}$$

$$H^{J^\pi}_{p'K'pK} \equiv \langle \hat{P}^{J^\pi}_{MK'}\Phi(\boldsymbol{Z}^{(p')}_1, ..., \boldsymbol{Z}^{(p')}_{N+1})|\hat{H}|\hat{P}^{J^\pi}_{MK}\Phi(\boldsymbol{Z}^{(p)}_1, ..., \boldsymbol{Z}^{(p)}_{N+1})\rangle, \tag{2.14}$$

$$N^{J^\pi}_{p'K'pK} \equiv \langle \hat{P}^{J^\pi}_{MK'}\Phi(\boldsymbol{Z}^{(p')}_1, ..., \boldsymbol{Z}^{(p')}_{N+1})|\hat{P}^{J^\pi}_{MK}\Phi(\boldsymbol{Z}^{(p)}_1, ..., \boldsymbol{Z}^{(p)}_{N+1})\rangle. \tag{2.15}$$

To describe complicated cluster structures, superposing a large number of various configurations is required. This becomes more difficult when the number of clusters increases. If we have a large enough number of $p_{\max}$, the GCM wave function Eq. (2.12) would depict the multi-cluster systems close to the real system. Then, it is essential to efficiently produce each pth set of the vectors which can make the computational time much less to superpose with as few numbers of basis as possible. For this reason, we exploit the REM [40] which generates wave functions in an efficient and natural way.

2.3 Real-time evolution method

In this section, we explain the framework of the real-time evolution method. It generates the pth set of the wave function as generating functions in Eq. (2.12) using the equation-of-motion (EOM). We apply the time-dependent variational principle with the wave function Eq. (2.4),

$$\delta \int dt \frac{\langle \Phi(\boldsymbol{Z}_1, ..., \boldsymbol{Z}_{N+1}) | i\hbar \, d/dt - \hat{H} | \Phi(\boldsymbol{Z}_1, ..., \boldsymbol{Z}_{N+1}) \rangle}{\langle \Phi(\boldsymbol{Z}_1, ..., \boldsymbol{Z}_{N+1}) | \Phi(\boldsymbol{Z}_1, ..., \boldsymbol{Z}_{N+1}) \rangle} = 0, \tag{2.16}$$

which leads to the EOM for the $N\alpha + 1$ cluster centroids $\boldsymbol{Z}_1, ..., \boldsymbol{Z}_{N+1}$,

$$i\hbar \sum_{j=1}^{N+1} \sum_{\sigma=x,y,z} C_{i\rho j\sigma} \frac{dZ_{j\sigma}}{dt} = \frac{\partial \mathcal{H}_{int}}{\partial Z^*_{i\rho}}, \tag{2.17}$$

$$\mathcal{H}_{int} \equiv \frac{\langle \Phi(\boldsymbol{Z}_1, ..., \boldsymbol{Z}_{N+1}) | \hat{H} | \Phi(\boldsymbol{Z}_1, ..., \boldsymbol{Z}_{N+1}) \rangle}{\langle \Phi(\boldsymbol{Z}_1, ..., \boldsymbol{Z}_{N+1}) | \Phi(\boldsymbol{Z}_1, ..., \boldsymbol{Z}_{N+1}) \rangle}, \tag{2.18}$$

$$C_{i\rho j\sigma} \equiv \frac{\partial^2 \ln \langle \Phi(\boldsymbol{Z}_1, ..., \boldsymbol{Z}_{N+1}) | \Phi(\boldsymbol{Z}_1, ..., \boldsymbol{Z}_{N+1}) \rangle}{\partial Z^*_{i\rho} \partial Z_{j\sigma}}, \tag{2.19}$$

where the j in the sum runs from 1 to $N + 1$ in Eq. (2.17), which denotes each centroid of the $3\alpha + n$ cluster. The set of the vectors $\{\boldsymbol{Z}_1, ..., \boldsymbol{Z}_{N+1}\}$ is obtained from the EOM as function of the real-time t, which denotes the wave function $\Phi(\boldsymbol{Z}_1(t), ..., \boldsymbol{Z}_{N+1}(t))$ at each time t corresponding to the pth set in Eq. (2.12). Here, the time-averaged expectation value of the wave functions $\Phi(\boldsymbol{Z}_1(t), ..., \boldsymbol{Z}_{N+1}(t))$ is equivalent to the canonical ensemble at the same excitation energy, which shows an ergodic property [41]. Also, the generated set of the wave functions follows quantum statistic although the motion of the wave packet centroids is classical [42].

We impose a rebound condition because the particles can move the unphysical region if they are not bound within some specific area during the time-evolving with a high excited intrinsic energy. The rebound condition we used is the quadratic

potential well [43] with the radius from the center of mass of the form

$$k\sum_i f(|\boldsymbol{D}_i - \boldsymbol{D}_{c.m.}|), \tag{2.20}$$

$$f(x) = (x-a)^2\theta(x-a), \tag{2.21}$$

$$\boldsymbol{D}_{c.m.} = \frac{4}{N+1}\sum_i^N \boldsymbol{D}_i + \frac{1}{N+1}\boldsymbol{D}_{N+1}, \tag{2.22}$$

where $\theta(x-a)$ is a step function with $\boldsymbol{D}_i = \mathrm{Re}\boldsymbol{Z}_i$, and $k = 1.5$ MeV/fm^2. The rebound radius a is set to make the farthest two particles 20 fm for the 2-body systems of ^{8}Be and ^{5}He. However, the rebound radius is set to 10 fm for ^{13}C. It is smaller than the cases of ^{8}Be and ^{5}He and the reason is that we do not treat the s-wave resonance states in this study, which requires a very large model space to describe the wave function, but it is large enough to treat the p-wave resonance states. Additionally, it does not affect confirming the band structures in ^{13}C with being confirmed that 8 and 12 fm of the rebound radii did not give any deviation to establishing the low-lying states and their band structures. Finally, we perform the GCM calculation with the generated basis set $\Phi(\boldsymbol{Z}_1(t), ..., \boldsymbol{Z}_{N+1}(t))$,

$$\Psi^{J\pi}_M(T_{\max}) = \int_0^{T_{\max}} dt \sum_{K=-J}^{J} \hat{P}^{J\pi}_{MK} f_K(t)\Phi(\boldsymbol{Z}_1(t), ..., \boldsymbol{Z}_{N+1}(t)), \tag{2.23}$$

where we integrate from the initial time to the total propagated time $T_{\max}$.

2.4 Multipole transitions and Weisscopf estimate

In this study, several observables with their operators are calculated. Firstly, the root-mean-square (r.m.s.) radius of the $N\alpha + 1$ system is given as,

$$R = \langle\Psi^{J\pi}|\frac{1}{A}\sum_{i=1}^{A}(\boldsymbol{r}_i - \boldsymbol{r}_{\mathrm{c.m.}})^2|\Psi^{J\pi}\rangle^{1/2}. \tag{2.24}$$

Similarly, the matrix element of the isoscalar monopole (IS0) transition strength is,

$$M(\mathrm{IS0}; J_i^\pi \to J_f^\pi) = \langle J_f^\pi | \sum_{i=1}^{A} (\boldsymbol{r}_i - \boldsymbol{r}_{\mathrm{c.m.}})^2 | J_i^\pi \rangle. \tag{2.25}$$

In the shell model, excited states are explained by the particle-hole excitation. Thus, the monopole excitation is estimated from the single-particle excitation. However, the cluster state is described by superposing many particle-hole excitation configurations, so one particle-hole excitation would be very small. The large monopole transition strength is a signature of the cluster state [44]. Also, as the radius and IS0 transition operator have the same form, a large transition strength implies that the excited state J_n^π could be a gas-like state. This will be exploited to investigate the Hoyle-analog state in Section 3.2.

Secondly, the electric quadrupole transition probabilities $B(E2)$ are calculated to prove the shape of each state, in which $B(E2)$ is sensitive to the deformation of nuclei. In particular, a rotational band is formed by a rotation of a rigid body, so the states in a rotational band show the same geometrical structure and are connected by the strong $E2$ transitions as explained in Ref. [30]. The transition probabilities $B(E2)$ with the transition operator is defined as,

$$B(E2; J_i \to J_f) = \sum_{M_f \mu} |\langle J_f M_f | e \sum_{i=1}^{A} (\boldsymbol{r}_i - \boldsymbol{r}_{\mathrm{c.m.}})^2 Y_{2\mu}(\boldsymbol{r}_i - \hat{\boldsymbol{r}}_{\mathrm{c.m.}}) \frac{1+\tau_z}{2} | J_i M_i \rangle|^2. \tag{2.26}$$

Thus-calculated transition probabilities are compared with the Weisscopf estimate that is calculated as,

$$B(EL) = \frac{(1.2)^{2L}}{4\pi} \Big(\frac{3}{L+3} \Big)^2 A^{2L/3} \; e^2 \mathrm{fm}^{2L}, \tag{2.27}$$

for a multipole L transition. This comparison provides information on whether a single particle participated in the transition. For example, the transition is accompanied by the collective motion rather than the single particle motion if the $B(E2)$

value is larger than the Weisscopf estimate.

2.5 Overlap between the single and GCM wave function

Since REM provides wave functions without any presumed spatial symmetry, it is worth evaluating if an arbitrary state exhibits triangular symmetry. In this study, the GCM wave function is formed by the superposition of a set of generated REM wave functions, in which each REM wave function has a different configuration. To measure the intrinsic structure of each eigenstate, we introduce the overlap between the superposed GCM wave function and the single basis wave function defined as,

$$O_i = \sum_{KK'} \langle \Psi^{J\pi}_M | P^{J\pi}_{MK} \Phi_i \rangle \, B^{-1}_{KK'} \, \langle P^{J\pi}_{MK'} \Phi_i | \Psi^{J\pi}_M \rangle \,, \tag{2.28}$$

where B^{-1} is the inverse matrix of B which is the overlap of projected basis wave functions,

$$B_{KK'} = \langle P^{J\pi}_{MK} \Phi_i | P^{J\pi}_{MK'} \Phi_i \rangle \,. \tag{2.29}$$

This overlap would provide which configuration is dominant. In addition, since the GCM wave function $\Psi^{J\pi}_M$ is a superposition of Φ_i [Eq. (2.12)], $\Psi^{J\pi}_M$ can be approximated by a single basis wave function Φ_i if the overlap O_i is large. Therfore, a state having a large overlap with a single basis wave function can be regarded as a rigid body state, so it is a good way to prove symmetry in nuclear systems.

2.6 Analytic continuation in the coupling constant

Here, we explain the ACCC method. The ACCC Hamiltonian H' is comprised as,

$$H'(\lambda) = H + \lambda H_a, \tag{2.30}$$

where H is the original Hamiltonian of the physical system and H_a is an auxiliary potential multiplied by the coupling constant λ. The Hamiltonian H', which is a function of the coupling constant λ, makes the resonance states unphysically bound with a large λ. Then, we extrapolate the original resonance states, where $H'(0) = H$, based on the momenta of their bound states. The resonance momentum k_l is estimated by the Padé series,

$$k_l(x) = i\,\frac{P_N(x)}{Q_M(x)} = i\,\frac{p_0 + p_1 x + p_2 x^2 + \cdots + p_N x^N}{1 + q_1 x + q_2 x^2 + \cdots + q_M x^M}. \tag{2.31}$$

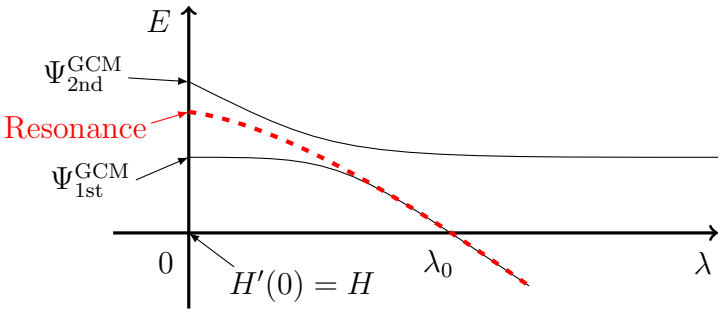

Figure 2.2: Scheme of ACCC

A schematic illustration of how ACCC works is shown in Fig. 2.2. The GCM wave functions treat resonance states using bound state approximation, and therefore, the GCM eigenstates above the threshold are usually contaminated with the continuum states. In the ACCC method, the resonance states become bound states by the attractive potential. The first state $\Psi^{\rm GCM}_{\rm 1st}$ is almost a continuum state at $\lambda = 0$, so it shows a horizontal line where λ is near 0. The second state $\Psi^{\rm GCM}_{\rm 2nd}$ consists of mainly resonance state, so it starts to decrease as λ gets larger from 0. There is a cross point where two states are close to each other, and after that, the resonance state and the continuum state are separated. The continuum state remains the horizontal line, in which the auxiliary potential does not affect the system since there is no interaction among the constituent particles. However, the resonance state is continuously decreasing as the potential is stronger with large λ and finally becomes a bound state when $\lambda > \lambda_0$. The bound states of the resonance have pure imaginary momenta, in which they can construct the Padé series as in Eq. (2.31).

The resonance state at $\lambda = 0$ is approximated by the thus-made analytic function shown as the red dashed line.

The variable x in Eq. (2.31) is defined following the behavior of the momentum as,

$$x = \sqrt{\lambda - \lambda_0} \quad \text{with} \quad k_l(\lambda_0) = 0. \tag{2.32}$$

The branch point λ_0 is the point of the coupling constant where the energy becomes 0, the threshold, for the $l > 0$ case. The Padé series in eq. (2.31) has the $N + M + 1$ coefficients and they are real since the function is constructed with the bound states. Then, the momentum k_l is to be the complex when $\lambda < \lambda_0$. As for the $l = 0$ case, λ_0 is not defined as the threshold, $k_0(\lambda_0) \neq 0$. The k_0 trajectory passes the negative imaginary axis, and the branch point is determined where $k_0(\lambda_0) = -i\mathrm{k}$, the kink point, and k_0 becomes to move on the fourth quadrant when $\lambda < \lambda_0$. An example of the $l = 0$ state can be found in Figure 3.6. Then, the resonance momentum k_l has the form as,

$$k_l = k_\mathrm{r} - ik_\mathrm{i}, \quad k_\mathrm{r} > 0, \quad k_\mathrm{i} > 0, \tag{2.33}$$

and from the resonance momentum k_l, the resonance energy E_R and the decay width Γ have following relations with the reduced mass m,

$$E = \frac{\hbar^2 k_l^2}{2m} \equiv E_R - i\Gamma/2, \quad E_R = \frac{\hbar^2}{2m}(k_\mathrm{r}^2 - k_\mathrm{i}^2), \quad \Gamma = \frac{2\hbar^2}{m} k_\mathrm{r} k_\mathrm{i}. \tag{2.34}$$

The resonance state and bound state are illustrated on the complex momentum plane in Figure 2.3. Resonance states are on the fourth quadrant having both real and complex numbers while bound states are on the positive imaginary axis that gives minus energies. However, resonance states with complex momentum would also have complex energies.

Furthermore, the matrix elements of various observables explained above can be

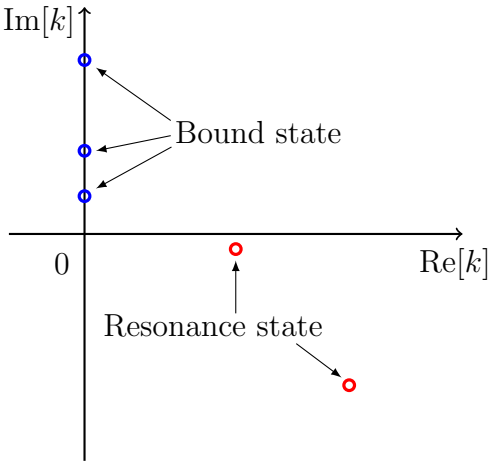

Figure 2.3: Concept of the bound state and the resonance state on the complex momentum plane.

also calculated within the ACCC framework [24],

$$(\Phi|\hat{O}|\psi\rangle = \underset{\lambda\to 1}{\text{Cont}} \int_0^\infty \Phi^*(k_l(\lambda), r) O\psi(r) dr, \tag{2.35}$$

where the round bra and angled ket denote the resonance and bound states, respectively. From the matrix elements calculated with the bound states ($\lambda > \lambda_0$), one can construct the Padé series and estimate in the same manner. The sign 'Cont' means the continuation of the coupling constant λ to the physical point. In this process, the normalization of the wave functions of the resonance states can be explained by Zel'dovich regularization, which mathematically redefines the overlap of two resonance wave functions, but leads to the same result with conventional integration [24].

Chapter 3

Results and discussion

3.1 Band Structure and Shape of ^{13}C

3.1.1 Time evolution of the $3\alpha + n$ system

The numerical calculations were performed according to the following procedure. First, using pure imaginary-time $\tau = it$ in Eq. (2.17), we calculate the minimum intrinsic energy, that is found to be -83.1 MeV. Then, we generate the wave functions with the intrinsic excitation energy $E^*_{\rm int}$ using the same equation. We have tested several excitation energies and used $E^*_{\rm int} = 30$ MeV in this work as it gives the best convergence of the GCM calculation. Using these wave functions as the initial condition at $t = 0$, we calculate the time evolution of the 3α+n system. The total propagation time was set to 10,000 fm/c, and the wave functions are recorded at every 33 fm/c. Consequently, an ensemble of the 300 wave functions is generated. By using different inital wave functions at $t = 0$, we generated two ensembles which we call set 1 and 2.

Several snapshots of the wave functions from these ensembles are shown in Fig. 3.1. Note that the wave functions of set 1 and 2 at $t = 0$ fm/c have different momenta of clusters, although they have almost the same spatial distributions. Consequently, the set 1 and 2 show the different results of the time evolution. We also note that various nuclear shapes with different cluster configurations naturally

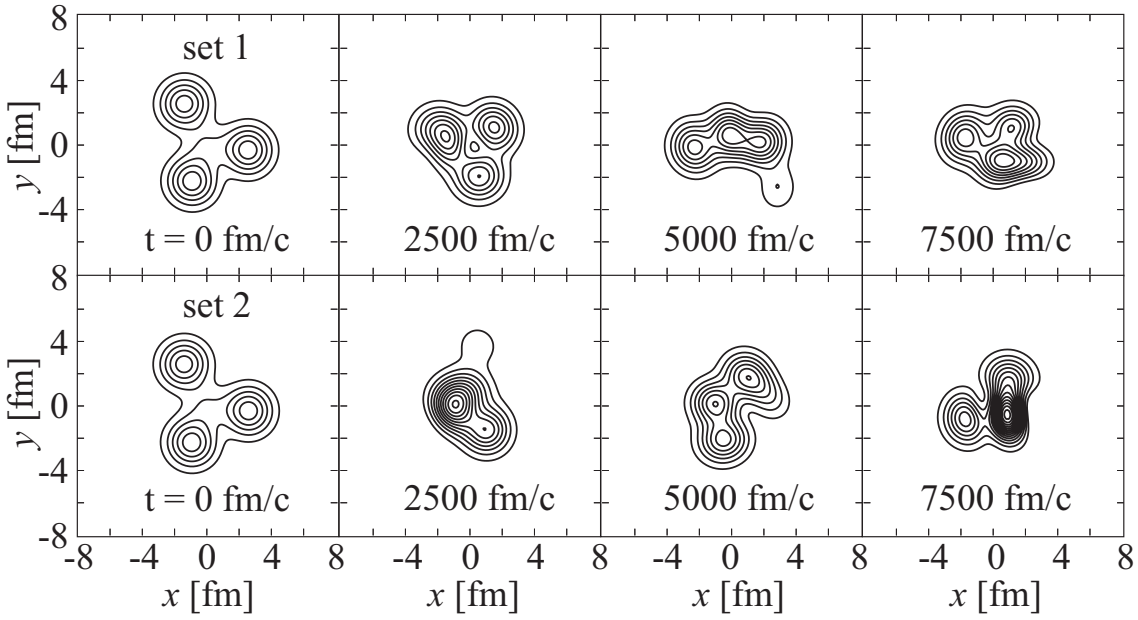

Figure 3.1: The snapshots of the intrinsic density distributions obtained by the real-time evolution. The top (bottom) panels show the wave functions from the ensemble set 1 (set 2).

emerge from the EOM. In some cases 3α particles are close to each other and the valence neutron is apart from them. In other cases, 2α particles and the valence neutron are close to each other, and an α particle is apart from others describing $^9\mathrm{Be}^* + \alpha$ like configurations. In this manner, the ensembles of the basis wave functions were prepared without any assumption of the spatial symmetry.

3.1.2 The calculated full spectrum

The generated wave functions are superposed to diagonalize the Hamiltonian. To confirm the convergence of the calculation, Fig. 3.2 shows the energies and radii of the $1/2^-_1$ and $5/2^+_1$ states, which are the lowest negative- and positive-parity stats, as functions of the propagation time T_{max}. The energy and radius of the ground state ($1/2^-_1$ state) show fast convergence and both sets reach almost the identical values. Thus, the obtained GCM wave functions are converged well independent of the initial wave functions. The figure also shows that REM yields approximately 1 MeV deeper binding energy of the $1/2^-_1$ state than the previous study by Furutachi

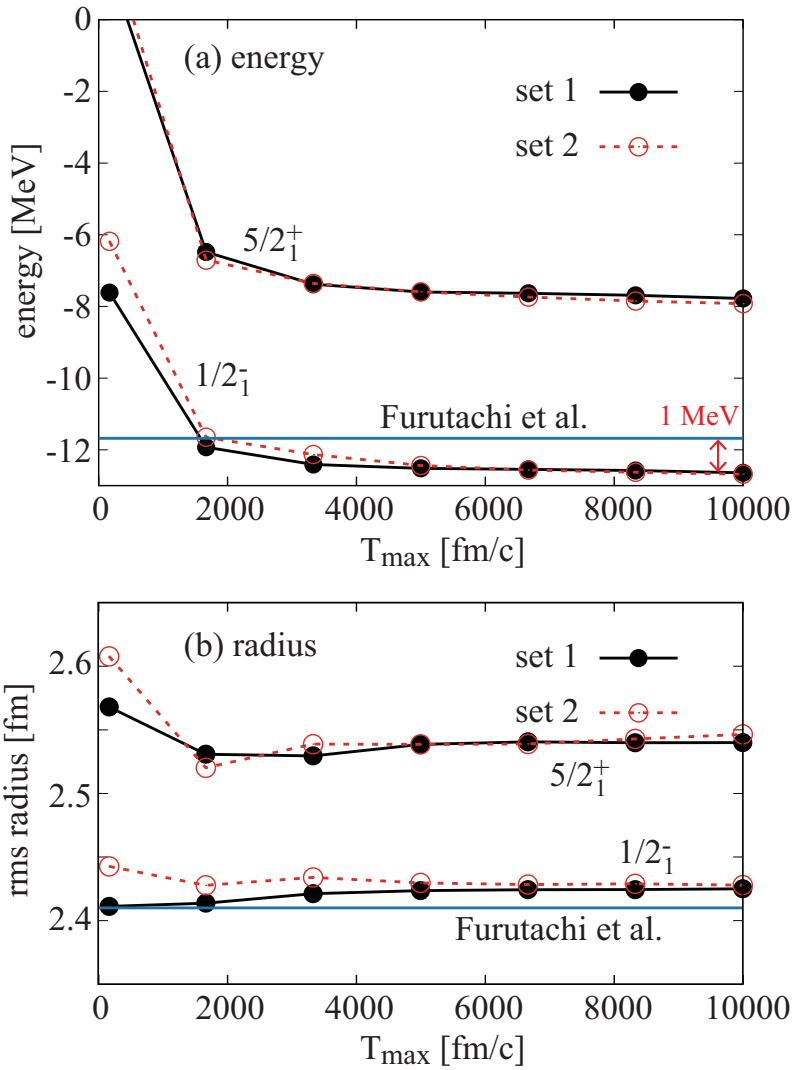

Figure 3.2: The energies and radii of the $1/2^-_1$ and $5/2^+_1$ states obtained from set 1 and 2 as a function of the total propagation time $T_{\rm max}$. The strength of the spin-orbit potential $u_{ls} = 2000$ MeV was adopted. The result for the $1/2^-_1$ state obtained in Ref. [15] are denoted by blue lines.

et al. [15] who used the same Hamiltonian. This clearly shows that REM can describe the 3α+n system more accurately. It is interesting to note that REM gives the larger radius of the ground state despite the deeper binding energy. This means that REM yields more stretched and long-ranged wave function. It is also noted that good convergence of the $5/2^+_1$ state was also achieved by using the same ensembles.

The left half of Fig. 3.3 compares the full spectrum obtained by REM and the negative-parity states calculated by Furutachi *et al.* [15]. Because two calculations

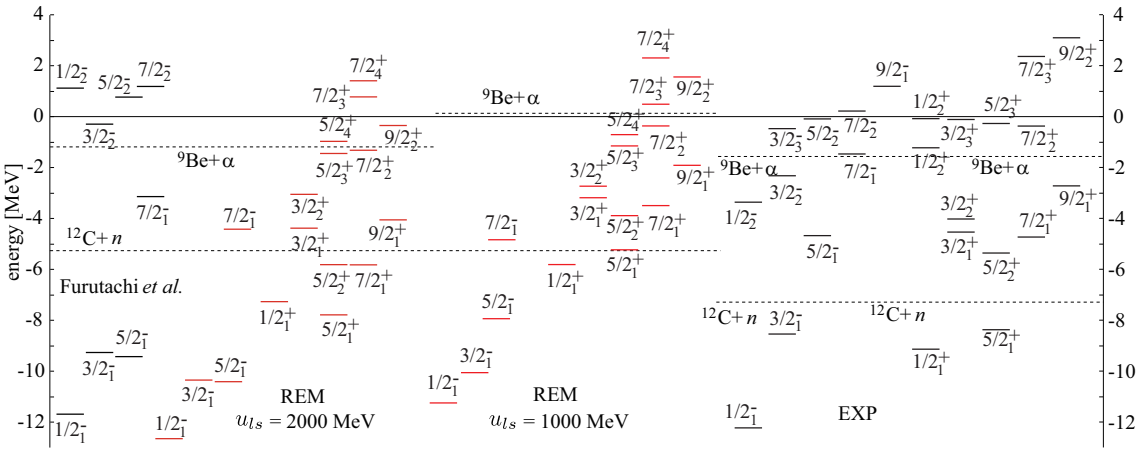

Figure 3.3: The energy spectrum of ^{13}C calculated by using the strength of the spin-orbit potential u_{ls}=2000 and 1000 MeV. The energy is measured relative to the $3\alpha + n$ threshold. The spectrum is compared with that obtained by Furutachi *et al.* [15] using the same Hamiltonian with u_{ls}=2000 MeV. Experimental data are taken from Ref. [45].

use the same Hamiltonian, deeper binding energy means a better description of the bound states below the neutron threshold. Obviously, the present calculation gives deeper energies to all the negative-parity states below the threshold ($1/2^-_1$, $3/2^-_1$ and $5/2^-_1$). It also gives deeper binding energy to the $7/2^-_1$ state located just above the threshold, to which the bound-state approximation may be validated. Thus, REM offers a better description of the bound states than ordinary GCM calculations.

However, the situation is different for the negative-parity resonances above the neutron threshold to which variational principle is not applicable and the bound-state approximation does not guarantee the energy convergence. In fact, two calculations disagree in the highly excited negative-parity states. It is noted that the model space of REM is much larger than that of the GCM by Furutachi *et al.* [15]. As a result, we found that most of the negative-parity resonances are coupled with the non-resonant continuum which makes it difficult for us to identify resonant solutions from many other non-resonant solutions. Therefore, we have not shown the negative-parity states above the neutron threshold in Fig. 3.3. On the contrary, although we cannot tell the reason clearly, we found that the coupling is not strong in the positive-parity states, and stable solutions are obtained which are plotted as

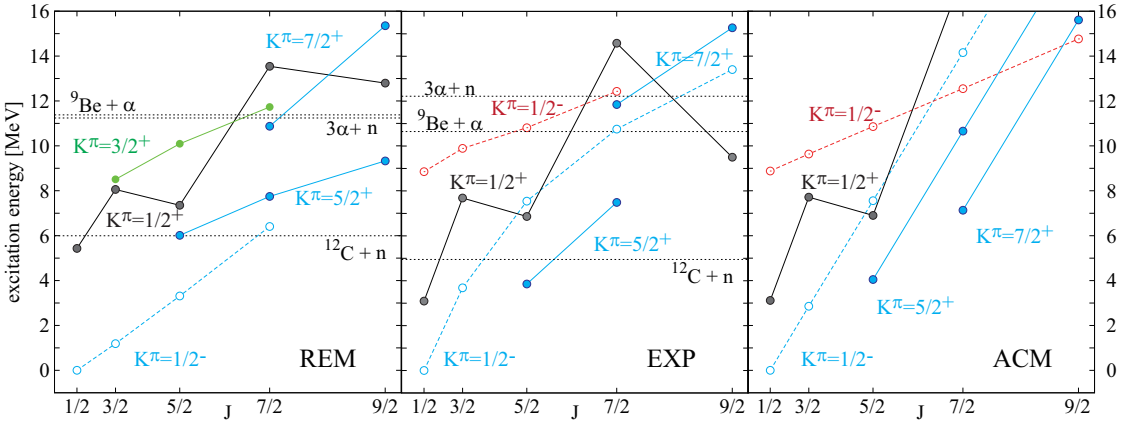

Figure 3.4: The band-assignment based on the calculated $E2$ transition strengths compared with that from the algebraic cluster model (ACM) [31] and the experimental assignment which was also tentatively proposed in Ref. [31]. The filled (open) symbols show the positive-parity (negative-parity) states.

resonances in the figure.

The spectrum obtained by the spin-orbit strength $u_{ls} = 2000$ MeV does not reproduce the order of the ground band spectrum. It underestimates the excitation energy of the $5/2^-_1$ state and the spectrum deviates from the observed rotational pattern. This may affect the assignment of the rotational bands and the discussion of the intrinsic shape. Therefore, we performed an additional calculation using weaker spin-orbit strength $u_{ls} = 1000$ MeV to check the interaction dependence of the spectrum. As seen in Fig. 3.3, the weaker spin-orbit strength yields the correct order of the ground band member states ($1/2^-_1$, $3/2^-_1$, $5/2^-_1$ and $7/2^-_1$ states), although it still overestimates the moment-of-inertia of the ground band. The side effect of the weaker spin-orbit interaction is the overestimation of the excitation energies of the positive-parity states. This may be due to the overestimation of the ^{9}Be+α threshold energy. If we measure them relative to the ^{9}Be+α threshold, the excitation energies of many positive-parity states get closer to the observed values. This implies that many positive parity-states have ^{9}Be+α structure [13, 14].

Table 3.1: The calculated intra- and inter-band $E2$ transition probabilities in the unit of $e^2\text{fm}^4$. The transitions larger than the Weisskopf estimate (1W.U. = 1.8 $e^2\text{fm}^4$) are shown. The numbers in the parenthesis are the experimental values.

band $K_i^\pi \to K_f^\pi$	J_i	J_f	$B(E2; J_i \to J_f)$
$1/2^- \to 1/2^-$	$1/2_1^-$	$3/2_1^-$	17.4 (12.7)
		$5/2_1^-$	17.1 (16.9)
	$3/2_1^-$	$5/2_1^-$	2.4
		$7/2_1^-$	17.8
	$5/2_1^-$	$7/2_1^-$	2.0
$5/2^+ \to 5/2^+$	$5/2_1^+$	$7/2_1^+$	13.8
		$9/2_1^+$	10.9
	$7/2_1^+$	$9/2_1^+$	12.0
$7/2^+ \to 7/2^+$	$7/2_2^+$	$9/2_3^+$	12.9
$1/2^+ \to 1/2^+$	$1/2_1^+$	$3/2_1^+$	16.7
		$5/2_2^+$	20.1
	$3/2_1^+$	$5/2_2^+$	5.0
		$7/2_4^+$	7.6
	$5/2_2^+$	$9/2_2^+$	9.9
$3/2^+ \to 3/2^+$	$3/2_2^+$	$5/2_3^+$	10.0
		$7/2_3^+$	8.7
	$5/2_3^+$	$7/2_3^+$	9.8
$5/2^+ \to 7/2^+$	$7/2_1^+$	$7/2_2^+$	4.3
$1/2^+ \to 5/2^+$	$1/2_1^+$	$5/2_1^+$	6.7 (9.0)
	$5/2_2^+$	$5/2_1^+$	3.6
		$7/2_1^+$	4.3
		$9/2_1^+$	3.3
	$9/2_2^+$	$7/2_1^+$	2.2
$1/2^+ \to 3/2^+$	$3/2_1^+$	$7/2_3^+$	2.3
	$7/2_4^+$	$5/2_3^+$	3.0
$3/2^+ \to 5/2^+$	$3/2_2^+$	$5/2_1^+$	2.7

3.1.3 Band assignment and shape of intrinsic states

Figure 3.4 presents the band assignment determined from the calculated $E2$ transition strengths listed in Tab. 3.1 and compares it with those from the experiment and the ACM calculation. The band assignment of the REM results is unambiguous as the intra-band $E2$ transitions are clearly stronger than the inter-band transitions.

The $K^\pi = 1/2^-$ band is built on the $1/2_1^-$ ground state. The intra-band $E2$ transition strengths are reasonably described and comparable with the experimental data for the $1/2_1^- \to 3/2_1^-$ and $1/2_1^- \to 5/2_1^-$ transitions. Experimentally, the ground

band terminates at the $9/2_1^-$ state, but we could not identify the corresponding state in our calculation. This may be due to the high excitation energy of this state which causes the strong coupling with the continuum and makes it difficult to separate this state within the bound-state approximation.

For the positive-parity states, we have assigned four rotational bands; $K^\pi = 5/2^+$, $7/2^+$, $1/2^+$ and $3/2^+$ which are built on the $5/2_1^+$, $7/2_2^+$, $1/2_1^+$ and $3/2_2^+$ states, respectively. Experimentally, the $E2$ transition strength for the $1/2_1^+ \to 5/2_1^+$ transition has already been measured (9.0 $e^2\text{fm}^4$) [45] and our calculation gives comparable value (6.7 $e^2\text{fm}^4$). However, no other $B(E2)$ data is available, and the positive-parity band assignment has not been firmly established by the experiments.

In Ref. [31], based on ACM which assumes the $3\alpha + n$ cluster structure with triangular symmetry, the authors proposed a band assignment (Fig. 3.4 right panel). They proposed the $K^\pi = 1/2^-$, $5/2^+$ and $7/2^+$ bands which share the same intrinsic structure, and the $K^\pi = 1/2^+$ and $1/2^-$ bands with different structure. They also tentatively classified the observed states into the rotational bands as shown in the middle panel of Fig. 3.4. Their assignment is similar to the present REM results in several aspects, but there are some differences as discussed below. First, both models suggest the ground $K^\pi = 1/2^-$ band and the excited $K^\pi = 5/2^+$ and $7/2^+$ bands, but the REM gives much larger moment-of-intertia of these bands while observed moment-of-inertia looks being in between the REM and ACM results. Second, both models also suggest $K^\pi = 1/2^+$ band, but we again see the disagreement in the moment-of-inertia. We will examine the structure of these bands in the following. Finally, the ACM proposed the excited $K^\pi = 1/2^-$ band as a "hoyle-like band" which has similar properties to the hoyle state of ^{12}C, but REM does not. This difference may be due to the bound state approximation made in the REM calculation which makes difficult to describe weakly interacting dilute resonances like the Hoyle state.

In addition to these four bands, they also pointed out the possible existence of a pair of the $K^\pi = 3/2^\pm$ band approximately at $E_x = 10$ MeV. Interestingly, the global structure of the four bands; $K^\pi = 1/2^-$, $5/2^+$, $5/2^+$ and $1/2^+$ qualitatively agrees with the REM results, although there exist several differences, for example,

Table 3.2: The calculated overlaps for each state which is defined by Eq. (2.28). The columns denoted by $O(1/2^-)$ and $O(1/2^+)$ show the overlap between REM wave function and the basis wave function which is most dominant in the $1/2^-_1$ and $1/2^+_1$ states, respectively.

	$K^\pi = 1/2^-$			$K = 1/2^+$	
J^π	$O(1/2^-_1)$	$O(1/2^+_1)$	J^π	$O(1/2^-_1)$	$O(1/2^+_1)$
$1/2^-_1$	0.83	0.12	$1/2^+_1$	0.14	0.58
$3/2^-_1$	0.83	0.16	$3/2^+_1$	0.18	0.56
$5/2^-_1$	0.73	0.06	$5/2^+_2$	0.25	0.56
$7/2^-_1$	0.76	0.13	$7/2^+_4$	0.35	0.25
			$9/2^+_2$	0.35	0.45
	$K^\pi = 5/2^+$			$K = 7/2^+$	
J^π	$O(1/2^-_1)$	$O(1/2^+_1)$	J^π	$O(1/2^-_1)$	$O(1/2^+_1)$
$5/2^+_1$	0.50	0.45	$7/2^+_2$	0.74	0.15
$7/2^+_1$	0.54	0.42	$9/2^+_3$	0.55	0.19
$9/2^+_1$	0.58	0.43			
	$K^\pi = 3/2^+$				
J^π	$O(1/2^-_1)$	$O(1/2^+_1)$			
$3/2^+_2$	0.45	0.40			
$5/2^+_3$	0.46	0.26			
$7/2^+_3$	0.35	0.28			

the order of the bands are different and several bands are missing. It is also noted that REM shows quantitatively better agreement with the experiment.

To confirm the intrinsic structure, the calculated overlaps by Eq. 2.28 are summarized in Tab. 3.2. The ground state has the maximum overlap, which is as large as 0.83, with the basis wave function shown in Fig. 3.5 (a). Note that the density distribution clearly shows the triangular configuration of 3α particles with a valence neutron where the lengths of the triangle are 3.31, 3.30 and 3.02 fm. Furthermore, we found that all the member states of the ground band have large overlaps no less than 0.70 with the same basis wave function. Therefore, we consider that the ground band is reasonably interpreted as the rotational band having a common intrinsic structure with a triangular symmetry as asserted by Bijker et al. [31]. They also argued that the $K^\pi = 5/2^+$ and $7/2^+$ bands have the same intrinsic structure and are classified as the "ground band". Indeed, we found that these bands have non-small overlap with the same basis wave function shown in Fig. 3.5 (a). However,

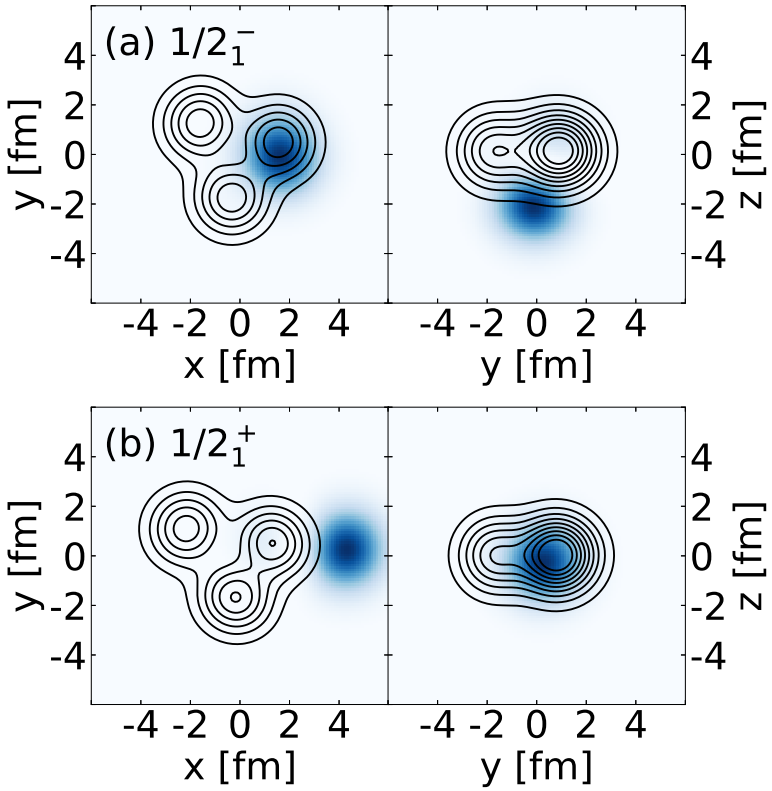

Figure 3.5: Panel (a): the density distribution of the basis wave functions which have the maximum overlap with the $1/2_1^-$ state. Panel (b): Same as panel (a) but for the $1/2_1^+$ state. Contours show the density of 3α particles and color plots show the density distribution of the valence neutron wave function.

our results show a deviation from a rigid shape. The magnitudes of the overlaps between these bands and the basis wave function shown in Fig. 3.5 (a) are reduced less than 0.60 except for the $7/2_2^+$ state. Furthermore, these bands have non-small overlaps with other configurations. For example, the $K^\pi = 5/2^+$ band has large overlap with the dominant basis wave function of the $1/2_1^+$ state, which is discussed below. Thus, the $K^\pi = 5/2^+$ and $7/2^+$ bands look similar to the $K^\pi = 1/2^-$ band, but the deviation from the rigid shape is not small.

In Ref. [31], the $K^\pi = 1/2^+$ band was assigned as a rotational band which also has a triangular arrangement of 3α particles but has the valence neutron in a different single-particle orbit. In the present calculation, we also found that the

band-head state ($1/2^+_1$ state) has the maximum overlap with a different basis wave function whose density distribution is shown in Fig. 3.5 (b), but has small overlap with the dominant configuration of the ground band [Fig. 3.5 (a)]. Apparently, the position of the wave packets of the valence neutron is different from that of the $1/2^+_1$ state, and α particles deviate from equilateral triangular arrangement as the lengths of the triangle are 3.55, 3.51 and 2.67 fm. This confirms that the $K^\pi = 1/2^+$ band has a different intrinsic structure. However, we again note that the magnitude of the maximum overlap is not as large as that of the ground band, and the member states of this band show the increasing mixture of other contributions as the excitation energy and angular momentum increase. In particular, the $7/2^+_4$ state has rather small overlap with the intrinsic state of its band head ($1/2^+_1$ state) despite the strong $E2$ transition to other band member state ($3/2^+_1$). This indicates that the structure of the $K^\pi = 1/2^+$ band is not as simple as a rigid rotor. Finally, we also found the strongest admixture of the various configurations in the $K^\pi = 3/2^+$ band which is a candidate of the band proposed in Refs. [13, 31]. This may be due to the highest high excitation energy of this band. We note that the use of the stronger spin-orbit interaction (u_{ls} = 2000 MeV) strength does not change most of the analysis discussed above. The only change caused by stronger spin-orbit interaction is the nature of the $K^\pi = 1/2^+$ band. As seen in Fig. 3.3, the $1/2^+_1$ state is more deeply bound by the stronger spin-orbit interaction, and hence, it tends to have more compact structure. Consequently, the overlaps $O(1/2^+_1)$ of the $K^\pi = 1/2^-$ and $7/2^+$ bands become larger. For example, the overlap between the $1/2^-_1$ ($7/2^+_2$) state and $1/2^+_1$ state increases to 0.57 (0.56). This indicates the $K = 1/2^+$ band structure approaches rigid-body due to deeper binding.

In short, the REM calculation confirmed that the ground band can be interpreted as a rigid-body rotational band which manifests the triangular symmetry. It also shows that ACM looks explaining the general trend of the excited bands. However, we found that all the excited bands have non-small admixture with other configurations and deviate from the rigid-body interpretation. One of the signature of this mixing is the non-small $E2$ transitions between the bands with different intrinsic

structures. Therefore, the experimental data for these transitions will provide us an important insight into the cluster structure of ^{13}C.

3.2 Resonance States of ^{13}C

3.2.1 Benchmark calculations of ACCC with REM

We first confirm the validity of combining the ACCC method with REM by performing benchmark calculations. As simple two-body systems, ^{8}Be(α+α) and ^{5}He(α+n) are compared with the preceding ACCC result by Tanaka *et al.* [25]. For the purpose, we employ the Minnesota force [46] and Reichstein and Tang spin-orbit interaction [47]. The Minnesota parameter for the physical system is chosen as $u = 0.94$ for ^{8}Be and $u = 0.98$ for ^{5}He and the α width parameter $\nu = 0.26$ is used following Tanaka *et al.* [25]. The zero-range limit for the spin-orbit interaction is taken, and the spin-orbit strength parameter $J_{ls} = 50$ MeV·fm^2 is introduced for the physical system. For the REM conditions, we use the intrinsic energies $\mathcal{H}_{int} = 13.8$ and 18 MeV for ^{8}Be and ^{5}He, respectively. These intrinsic energies make the constituent particles move all the physical model space, but not to highly excited so that they can give a good convergence of the GCM calculation. The superposed number of wave functions are 75(90) for ^{8}Be(^{5}He).

In this benchmark calculations, the Minnesota parameter u is exploited as the coupling constant λ. When u gets larger than the physical points, then the Minnesota force is subsequently introduced as the auxiliary potential in ACCC, which makes the resonance states bound. It is noted that we use an α cluster model and increasing u as λ does not affect the structure of the α particle.

Their results are listed in Table. 3.3. The 0^+ and 2^+ states of ^{8}Be are consistent with the results of Tanaka *et al.* [25], and we additionally tested the 4^+ state that is comparable to the experimental value. As for the ^{5}He case, the spin-orbit interaction is included in the Hamiltonian so that the p-wave state is split and their splitting is also well reproduced in our framework. The s-wave state of ^{5}He, which has very

large width, is also properly described compared to the preceding ACCC result although the calculation of the Padé approximation to the s-wave state is naturally unstable. The exceptional kink point of the s-wave state is depicted in Fig. 3.6. The momentum trajectory moves on the positive imaginary axis for the bound states and it goes further to the negative imaginary axis for a while then it starts to have both the real and imaginary components from where we call the kink point. In the fourth quadrant, it first passes the $k_r < k_i$ region, which is unphysical since $E_R < 0$, and it finally becomes the physical resonance at $u = 0.98$. On the other hand, the trajectory simply goes to the fourth quadrant from the threshold point for $l > 0$ cases.

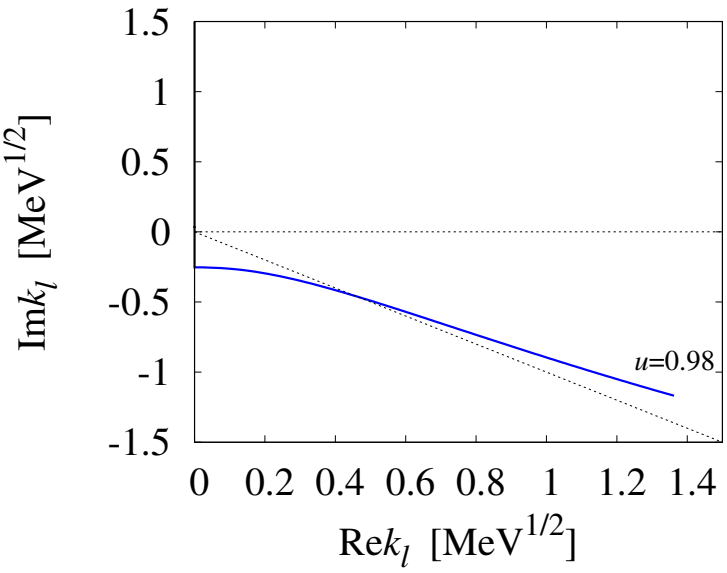

Figure 3.6: The momentum trajectory of the $1/2^+$ resonance of ^{5}He.

From the comparison of the simple two 2-body systems, we have confirmed the nucleon-nucleon and the spin-orbit interactions working in our ACCC calculation based on the REM framework. Furthermore, we adopt the spin-orbit interaction as the auxiliary potential, which is a new methodological trial of ACCC. In this case, the spin-orbit strength J_{ls} is selected as the coupling constant. It was applied to ^{5}He and the resonance parameters of the $1/2^-$ and $3/2^-$ states were obtained as follows: $0.77 - i0.22$ and $2.00 - i2.52$, respectively. The comparison between the

Table 3.3: Benchmark calculations of the resonance energy E_R and the decay width Γ of ^{8}Be and ^{5}He obtained by the ACCC method compared with the previous study. Units are in MeV.

		REM		Tanaka *et al.*		EXP	
	J^π	E_R	Γ	E_R	Γ	E_R	Γ
^{8}Be	0^+	0.224	0.001	0.208	0.003	0.09184	5.57 ± 0.25 eV
	2^+	2.87	1.42	2.85	1.44	3.1218	1.513 ± 0.015
	4^+	11.77	4.82			11.44	≈ 3.5
^{5}He	$3/2^-$	0.78	0.66	0.77	0.64	0.735	0.648
	$1/2^-$	1.98	5.62	1.98	5.4	2.005	5.57
	$1/2^+$	12.7	163	12	180		

cases of central force and spin-orbit interaction as an example of the $3/2^-$ state is shown in Fig. 3.7. One can see that within the same energy region, the GCM result slowly starts to bound and then sharply increase the binding energy in the spin-orbit interaction case. Although the different choices of the auxiliary potential result in the different shape of the Padé function, we can reach the reasonable results in both cases. We expect that this novel way using a spin-orbit interaction will make the systems simpler when we want to treat the nuclear systems with non-spin-orbit interacting core.

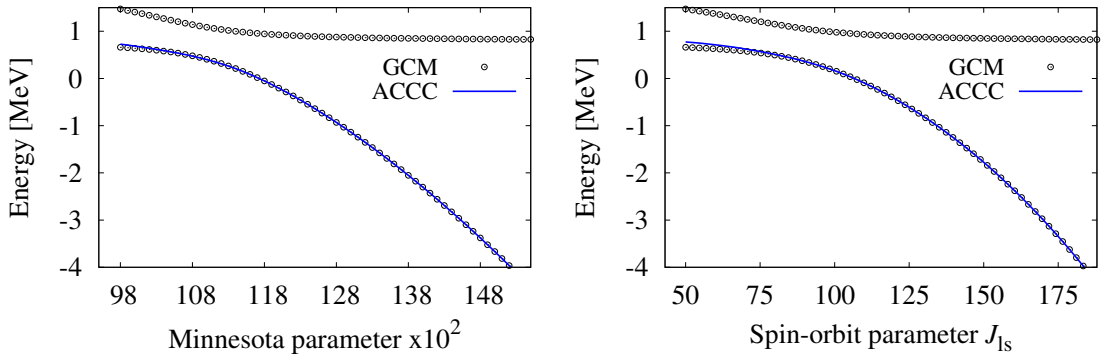

(a) $\lambda = u$ (b) $\lambda = J_{ls}$

Figure 3.7: $3/2^-$ state of ^{5}He using different interaction as an auxiliary potential. Panel (a) and (b) are the results with the central force (Minnesota parameter u as λ) and the spin-orbit interaction (strength parameter J_{ls} as λ), respectively.

3.2.2 Resonance states of the $1/2^-$ states in ^{13}C

^{13}C is described as the 4-body system of $3\alpha + n$ in the REM framework. If we adopt the central force as the auxiliary potential for the ACCC calculation, ^{13}C becomes to bound than ^{12}C with very large coupling constant λ because ^{12}C is also getting large binding energy among the α particles as λ being larger. Consequentially, the energy difference between the bound state of the resonance and ^{12}C is too small to construct the Padé approximation. However, as we proposed and demonstrated above, we use the spin-orbit interaction as the attractive potential, which makes ^{13}C a simple 2-body system of $^{12}\mathrm{C} + n$. In this case, the energy of ^{12}C remains constant and the ground state of ^{12}C is set to the threshold for the ACCC calculation. Then, the resonance parameters are determined to the $^{12}\mathrm{C} + n$ decay channel. The momentum is calculated as $k_l = \sqrt{E(^{13}\mathrm{C}) - E(^{12}\mathrm{C}_{\mathrm{g.s.}})}$ and thus-obtained resonance energy and width are relative to the $^{12}\mathrm{C} + n$ threshold, but we will calculate other physical quantities such as radii and monopole transitions using the ACCC method that are not affected by the threshold so that we can rather easily investigate the Hoyle-analog state with the new approach. Such quantities will be calculated as explained in Eq. (2.35).

The Volkov No.2 and G3RS interactions are used for ^{13}C following our previous ^{13}C study in the previous section. The Majorana parameter M is fixed to 0.592 for the physical system in this work, which reproduces the excitation energy of the Hoyle state as 7.68 MeV (experimentally 7.65 MeV). The α width parameter is defined as $\nu = 1/2b^2$ and we set $b = 1.46$ fm, which gives the observed α particle's size and used also in our previous work. As for the REM conditions, two intrinsic energies are used for ^{13}C, $\mathcal{H}_{int} = 30$ and 40 MeV, to cover the various configurations of the resonance states of ^{13}C because 30 MeV, which was used in our previous work, gave good convergence and configurations for the low-lying states but it was not enough for the highly excited resonance states. We prepared 300 wave functions of each intrinsic energy in a total of 600 to be superposed.

Fig. 3.8 shows the $1/2^-$ states obtained by the Padé approximation. Here, we

have 2 choices of the physical point of the spin-orbit strength, V_{ls} = 1000 and 3000 MeV. The former reasonably reproduced spin-orbit splitting of ^{5}He and showed the correct order of the ground band and the lowest positive state in our previous work. The later can describe all the excited $1/2^-$ states as seen in the figure. The numerical results of them together with other quantities obtained by Eq. (2.35) are summarized in Table 3.4 and 3.5.

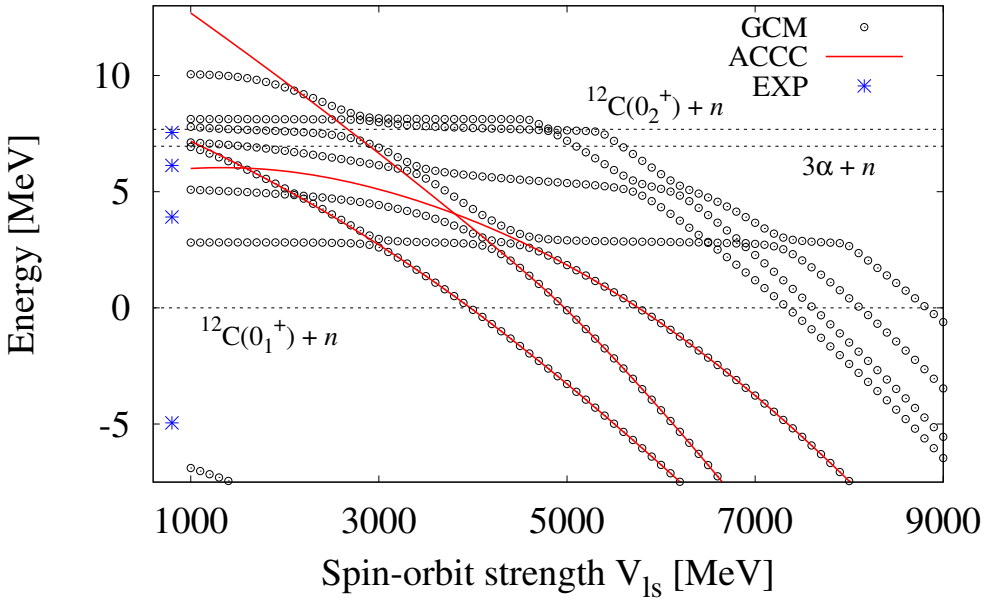

Figure 3.8: The $1/2^-$ resonance states obtained by the Padé approximation.

Table 3.4: Numerical results of the $1/2^-$ states are listed. Energies E from the threshold, widths Γ of resonance states, electric ($E0$) and isoscalar ($IS0$) monopole transition densities, and matter R_m and proton R_p radii with the choice of V_{ls} = 1000 MeV. Energy and width are in MeV, monopole transitions are in (e)fm^2, and radii are in fm.

	ACCC						EXP		
J^π	E	Γ	M($IS0$)	M($E0$)	R_m	R_p	E	Γ	M($IS0$)
$1/2^-_1$	−6.89	-	-	-	2.42	2.37	−4.95	-	-
$1/2^-_2$							3.91	0.15	6.1
$1/2^-_3$	6.00	1.26	15.26	6.37	3.01	2.88	6.13	<0.004	4.2
$1/2^-_4$	7.17	0.57	7.48	3.56	2.87	2.77	7.55	-	4.9
$1/2^-_5$	12.69	7.65	5.30	2.43	3.00	2.90			

Table 3.5: Same as Table 3.4 but with the choice of V_{ls} = 3000 MeV.

	ACCC						EXP		
J^π	E	Γ	M($IS0$)	M($E0$)	R_m	R_p	E	Γ	M($IS0$)
$1/2^-_1$	-10.39	-	-	-	2.38	2.34	-4.95	-	-
$1/2^-_2$	2.71	0.047	7.56	3.50	2.85	2.70	3.91	0.15	6.1
$1/2^-_3$	5.10	0.21	13.61	4.79	2.87	2.51	6.13	<0.004	4.2
$1/2^-_4$	6.65	2.41	9.52	4.78	2.78	2.73	7.55	-	4.9

In the case of V_{ls} = 1000 MeV, the 2nd state is not described in our cluster model, and it might have a shell model structure. The 3rd and 4th resonance energies are obtained in well agreement with the experiment, but their widths are orders of magnitude different. It is due to the weak spin-orbit strength, in which the resonance parameters are determined relative to the ^{12}C and the neutron in our ACCC framework. Their difference becomes smaller in the V_{ls} = 3000 MeV case. As for the 5th state, it is too highly excited state in the choice of V_{ls} = 1000 MeV, so we do not discuss in detail here as it is not in our scope to search for the Hoyle-analog state.

As explained above, the isoscalar monopole ($IS0$) transitions are obtained within the ACCC method, and they show the large transition strengths in all the excited $1/2^-$ states as in the experiment. At the same time, the electric monopole ($E0$) transitions also have about half times of each $IS0$ strength, which means the spatial excitation of protons is almost same as of neutrons and they have clear alpha cluster structures. All the excited states have large matter and proton radii compared to the ground state.

In the case of V_{ls} = 3000 MeV, the energies of all the excited states are properly described with the decay widths reduced to much smaller. The $IS0$ and $E0$ transitions again show large values implying these states are spatially developed. The radii are smaller than the V_{ls} = 1000 MeV case, and especially, the proton radius of the 3rd state is much smaller. The matter radius is still large as 2.87 fm, in which this state could have spatially distributed valence neutron with the ^{12}C core. The 4th state reveals that their matter and proton radii have similar size. If we recall

the V_{ls} = 1000 MeV case, the 4th state also had similar radii to each other. Furthermore, the radii and monopole transitions of the 4th state are almost consistent regardless of the choice of V_{ls}. We can regard that this state could be the candidate of the Hoyle-analog state in the $1/2^-$ states of ^{13}C. Here, it should be noted that the radius 2.87 fm is smaller than that of the Hoyle state, which is around 3.4 fm, but it is reasonable when we consider the role of the valence neutron as a glue to shrink the 3α particles.

The physical point between the two choices of V_{ls} should be the 1000 MeV case as it gives more natural description for ^{13}C including the ground state and the others even though the 2nd excited state is missing. however, we could explore detailed characteristics of the resonance states from V_{ls} = 3000 MeV so that we can suggest the $1/2^-_4$ state as a new candidate of the Hoyle-analog state, which is located above the $3\alpha + n$ threshold with V_{ls} = 1000 MeV. Additionally, the recent experimental study by Inaba *et al.* [18] found that there is a bump structure, which is composed of several states located closely to each other, around 12.5 MeV from the ground state (the 4th exp. state in our tables), and the bump structure, especially its IS0 transitions, was not described by the shell model calculation. Actually, they thought it could be the Hoyle-analog state in the beginning, but they concluded that it would not be the Hoyle-anaolg state due to other theoretical studies of the orthogonality condition mode (OCM) and the antisymmetrized molecular dynamics (AMD). This work will provide another possibility to find out the Hoyle-analog state in ^{13}C.

Chapter 4

Summary

In summary, we have first investigated the structure of the $3\alpha + n$ system by extending the REM framework. As a benchmark calculation for the $3\alpha + n$ system, REM well reproduced the ground and excited energies where we followed the same Hamiltonian of the previous study as a comparison. It was also demonstrated that REM accurately describes the wave functions which yields to the deeper binding energies.

We have also discussed the rotational band assignment and investigated if they manifest the triangular symmetry. The proposed band assignment qualitatively explains the observed data, although the order of several bands disagrees and the $K^\pi = 1/2^-$ band is missing in the present result. From the analysis of the overlap with the basis wave functions, it was found that the ground band can be regarded as a rigid-body rotational band which manifests the triangular symmetry. We also have seen that the triangular symmetry approximately explains the general nature of the excited bands. However, all the excited bands have non-small admixture with other configurations without symmetry and deviate from the rigid-body interpretation, because of their high excitation energies and angular momenta. The non-small $E2$ transitions between different bands are a signature of the configuration mixing, and we expect that the experimental data for these transitions will provide us an important information about the underlying symmetry behind the observed

spectrum.

In subsequent, the resonance states of the $1/2^-$ states in ^{13}C have been investigated. As a benchmark calculations to demonstrate the combination of ACCC and REM with the employed interactions, ^{8}Be and ^{5}He resonance states were well reproduced compared to the preceding ACCC study. In addition, a tactical treatment of ACCC was introduced, in which the spin-orbit interaction and its strength V_{ls} was exploited as the attractive potential and the coupling constant λ respectively in the ACCC framework and tested to the ^{5}He resonance states.

Based on this new treatment, the resonance states of ^{13}C were clearly figured out from the continuum. The matrix elements of radius and monopole transitions were also calculated within the ACCC framework, which provides cluster characteristics of each resonance state. The physical interaction was chosen with the spin-orbit strength $V_{ls} = 1000$ that reproduced spin-orbit splitting of ^{5}He and used in the Hamiltonian of Section 3.1. The $1/2^-_2$ state was not obtained in this study that means this state is definitely not an α cluster state. After comparison between the choices of $V_{ls} = 1000$ and 3000 MeV, the $1/2^-_3$ state was concluded to have a loosely bound neutron with the ^{12}C core since it showed large neutron radius with relatively small proton radius. In last, the $1/2^-_4$ state is concluded to be the possible candidate of the Hoyle-analog state in ^{13}C.

Acknowledgements

I first would like to acknowledge my supervisor, Prof. M. Kimura. I also thank Prof. B. Zhou and Prof. Q. Zhao for their advice and for many discussions. I thank Prof. W. Horiuchi, Prof. T. Kobayashi, and Prof. Y. Hirabayashi for their reviews and comments on my thesis. Prof. K. Kato helped me to understand the ACCC framework. During the doctoral period, I worked on the development of the EXFOR database, and I would like to thank Prof. M. Aikawa and Dr. N. Otsuka to work with them. Discussions with Dr. H. Motoki and Dr. H. Moriya, who receive Ph.D. with me, were insightful and interesting and widened my sight in nuclear physics. I appreciate all the other members of the theoretical nuclear physics laboratory. I am always grateful for my family's understanding and support. I particularly would like to express my thank and respect to Hyunguk Shin and Mijeom Back, my parents. Finally, I thank my friends in Korea.

During my doctoral period, I was partially supported by Hokkaido University DX Doctoral Fellowship. Section 3.1 was written based on our published work [Phys. Rev. C **103**, 054313 (2021)]. The calculations in this thesis were mainly performed on a supercomputer at Research Center for Nuclear Physics, Osaka University.

Bibliography

[1] F. Hoyle, The Astrophysical Journal Supplement Series **1**, 121 (1954).

[2] A. Tohsaki, H. Horiuchi, P. Schuck, and G. Röpke, Physical Review Letters **87**, 192501 (2001).

[3] T. K. Wheldon, Journal of Physics: Conference Series **639**, 012003 (2015).

[4] T. Wakasa, E. Ihara, K. Fujita, Y. Funaki, K. Hatanaka, H. Horiuchi, M. Itoh, J. Kamiya, G. Röpke, H. Sakaguchi, et al., Physics Letters B **653**, 173 (2007).

[5] Y. Funaki, T. Yamada, H. Horiuchi, G. Röpke, P. Schuck, and A. Tohsaki, Physical Review Letters **101**, 082502 (2008).

[6] S. Adachi, Y. Fujikawa, T. Kawabata, H. Akimune, T. Doi, T. Furuno, T. Harada, K. Inaba, S. Ishida, M. Itoh, et al., Physics Letters B **819**, 136411 (2021).

[7] N. Itagaki, S. Okabe, K. Ikeda, and I. Tanihata, Physical Review C **64**, 143011 (2001).

[8] T. Suhara and Y. Kanada-En'yo, Physical Review C **82**, 044301 (2010).

[9] H. Yamaguchi, D. Kahl, S. Hayakawa, Y. Sakaguchi, K. Abe, T. Nakao, T. Suhara, N. Iwasa, A. Kim, D. H. Kim, S. M. Cha, M. S. Kwag, J. H. Lee, E. J. Lee, K. Y. Chae, Y. Wakabayashi, N. Imai, N. Kitamura, P. Lee, J. Y. Moon, K. B. Lee, C. Akers, H. S. Jung, N. N. Duy, L. H. Khiem, and C. S. Lee, Physics Letters B **766**, 11 (2017).

[10] J. Li, Y. L. Ye, Z. H. Li, C. J. Lin, Q. T. Li, Y. C. Ge, J. L. Lou, Z. Y. Tian, W. Jiang, Z. H. Yang, J. Feng, P. J. Li, J. Chen, Q. Liu, H. L. Zang, B. Yang, Y. Zhang, Z. Q. Chen, Y. Liu, X. H. Sun, J. Ma, H. M. Jia, X. X. Xu, L. Yang, N. R. Ma, and L. J. Sun, Physical Review C **95**, 021303 (2017).

[11] T. Baba and M. Kimura, Physical Review C **97**, 054315 (2018).

[12] Y. Liu, Y. L. Ye, J. L. Lou, X. F. Yang, T. Baba, M. Kimura, B. Yang, Z. H. Li, Q. T. Li, J. Y. Xu, Y. C. Ge, H. Hua, J. S. Wang, Y. Y. Yang, P. Ma, Z. Bai, Q. Hu, W. Liu, K. Ma, L. C. Tao, Y. Jiang, L. Y. Hu, H. L. Zang, J. Feng, H. Y. Wu, J. X. Han, S. W. Bai, G. Li, H. Z. Yu, S. W. Huang, Z. Q. Chen, X. H. Sun, J. J. Li, Z. W. Tan, Z. H. Gao, F. F. Duan, J. H. Tan, S. Q. Sun, and Y. S. Song, Physical Review Letters **124**, 192501 (2020).

[13] M. Milin and W. Von Oertzen, European Physical Journal A **14**, 295 (2002).

[14] M. Freer, N. I. Ashwood, N. Curtis, A. Di Pietro, P. Figuera, M. Fisichella, L. Grassi, D. Jelavić Malenica, T. Kokalova, M. Koncul, T. Mijatović, M. Milin, L. Prepolec, V. Scuderi, N. Skukan, N. Soić, S. Szilner, V. Tokić, D. Torresi, and C. Wheldon, Physical Review C **84**, 034317 (2011).

[15] N. Furutachi and M. Kimura, Physical Review C **83**, 021303 (2011).

[16] T. Yamada and Y. Funaki, Physical Review C **92**, 034326 (2015).

[17] Y. Chiba and M. Kimura, Physical Review C **101**, 024317 (2020).

[18] K Inaba, Y Sasamoto, T Kawabata, M Fujiwara, Y Funaki, K Hatanaka, K Itoh, M Itoh, K Kawase, H Matsubara, et al., Progress of Theoretical and Experimental Physics **2021**, 093D01 (2021).

[19] Y. Funaki, H. Horiuchi, W. Von Oertzen, G. Röpke, P. Schuck, A. Tohsaki, and T. Yamada, Physical Review C **80**, 064326 (2009).

[20] T. Kawabata, Y. Sasamoto, M. Fujiwara, H. Hashimoto, K. Hatanaka, K. Itoh, M. Itoh, Y. Kanada-En'yo, K. Kawase, Y. Maeda, et al., in Journal of physics: conference series, Vol. 111, 1 (IOP Publishing, 2008), p. 012013.

[21] T. Yamada and Y. Funaki, Physical Review C **92**, 034326 (2015).

[22] K. Ikeda, N. Takigawa, and H. Horiuchi, Progress of Theoretical Physics Supplement **68**, 464 (1968).

[23] C. W. Hsu, B. Zhen, A. D. Stone, J. D. Joannopoulos, and M. Soljačić, Nature Reviews Materials **1**, 1 (2016).

[24] V. I. Kukulin, V. Krasnopolsky, and J Horácek, *Theory of resonances: principles and applications*, Vol. 3 (Springer Science & Business Media, 2013).

[25] N. Tanaka, Y. Suzuki, K. Varga, and R. Lovas, Physical Review C **59**, 1391 (1999).

[26] R. Imai, T. Tada, and M. Kimura, Physical Review C **99**, 064327 (2019).

[27] R. Bijker and F. Iachello, Physical Review C **61**, 067305 (2000).

[28] V. Della Rocca, R. Bijker, and F. Iachello, Nuclear Physics A **966**, 158 (2017).

[29] R. Bijker and F. Iachello, Progress in Particle and Nuclear Physics **110**, 103735 (2020).

[30] D. Marin-Lambarri, R. Bijker, M. Freer, M. Gai, T. Kokalova, D. Parker, and C. Wheldon, Physical Review Letters **113**, 012502 (2014).

[31] R. Bijker and F. Iachello, Physical Review Letters **122**, 162501 (2019).

[32] S. Shin, B. Zhou, and M. Kimura, Physical Review C **103**, 054313 (2021).

[33] S. Shin, B. Zhou, and M. Kimura, Few-Body Systems **62**, 1 (2021).

[34] A. Volkov, Nuclear Physics **74**, 33 (1965).

[35] N. Yamaguchi, T. Kasahara, S. Nagata, and Y. Akaishi, Progress of Theoretical Physics **62**, 1018 (1979).

[36] D. Brink and C. Bloch, *Proceedings of the international school of physics "enrico fermi" course xxxvi*, 1966.

[37] N. Furutachi and M. Kimura, Physical Review C **83**, 021303 (2011).

[38] P. Ring and P. Schuck, *The nuclear many-body problem* (Springer Science & Business Media, 2004).

[39] D. L. Hill and J. A. Wheeler, Physical Review **89**, 1102 (1953).

[40] R. Imai, T. Tada, and M. Kimura, Physical Review C **99**, 064327 (2019).

[41] J. Schnack and H. Feldmeier, Nuclear Physics A **601**, 181 (1996).

[42] A. Ono and H. Horiuchi, Physical Review C **53**, 2341 (1996).

[43] A. Ono and H. Horiuchi, Physical Review C **53**, 845 (1996).

[44] T. Yamada, Y. Funaki, H. Horiuchi, K. Ikeda, and A. Tohsaki, Progress of Theoretical Physics **120**, 1139 (2008).

[45] F. Ajzenberg-Selove, Nuclear Physics A **523**, 1 (1991).

[46] D. Thompson, M. LeMere, and Y. Tang, Nuclear Physics A **286**, 53 (1977).

[47] I. Reichstein and Y. Tang, Nuclear Physics A **158**, 529 (1970).